

# Suppressing Counter-Rotating Errors for Fast Single-Qubit Gates with Fluxonium

David A. Rower,<sup>1,2,\*</sup> Leon Ding,<sup>1,2,†</sup> Helin Zhang,<sup>2</sup> Max Hays,<sup>2</sup> Junyoung An,<sup>2,3</sup> Patrick M. Harrington,<sup>2,‡</sup> Ilan T. Rosen,<sup>2</sup> Jeffrey M. Gertler,<sup>4</sup> Thomas M. Hazard,<sup>4</sup> Bethany M. Niedzielski,<sup>4</sup> Mollie E. Schwartz,<sup>4</sup> Simon Gustavsson,<sup>2,§</sup> Kyle Serniak,<sup>2,4</sup> Jeffrey A. Grover,<sup>2</sup> and William D. Oliver<sup>1,2,3,¶</sup>

<sup>1</sup>*Department of Physics, Massachusetts Institute of Technology, Cambridge, MA 02139, USA*

<sup>2</sup>*Research Laboratory of Electronics, Massachusetts Institute of Technology, Cambridge, MA 02139, USA*

<sup>3</sup>*Department of Electrical Engineering and Computer Science,*

*Massachusetts Institute of Technology, Cambridge, MA 02139, USA*

<sup>4</sup>*Lincoln Laboratory, Massachusetts Institute of Technology, Lexington, MA 02421, USA*

(Dated: June 13, 2024)

Qubit decoherence unavoidably degrades the fidelity of quantum logic gates. Accordingly, realizing gates that are as fast as possible is a guiding principle for qubit control, necessitating protocols for mitigating error channels that become significant as gate time is decreased. One such error channel arises from the counter-rotating component of strong, linearly polarized drives. This error channel is particularly important when gate times approach the qubit Larmor period and represents the dominant source of infidelity for sufficiently fast single-qubit gates with low-frequency qubits such as fluxonium. In this work, we develop and demonstrate two complementary protocols for mitigating this error channel. The first protocol realizes circularly polarized driving in circuit quantum electrodynamics (QED) through simultaneous charge and flux control. The second protocol—commensurate pulses—leverages the coherent and periodic nature of counter-rotating fields to regularize their contributions to gates, enabling single-qubit gate fidelities reliably exceeding 99.997%. This protocol is platform independent and requires no additional calibration overhead. This work establishes straightforward strategies for mitigating counter-rotating effects from strong drives in circuit QED and other platforms, which we expect to be helpful in the effort to realize high-fidelity control for fault-tolerant quantum computing.

## I. INTRODUCTION

Superconducting qubits have emerged as a leading contender for performing quantum computation [1], with steadily increasing circuit sizes and rising gate fidelities approaching the levels required to begin scaling error correcting codes [2–6]. However, gate fidelities must improve further to realize useful quantum computations, e.g., by surpassing code thresholds to yield algorithmically-relevant logical error rates [6–9].

Decoherence poses a significant challenge to the realization of high-fidelity gates, contributing an error proportional to  $t_g/T_{\text{coh}}$ , where  $t_g$  represents the duration of a gate operation and  $T_{\text{coh}}$  the relevant coherence timescale. For superconducting qubits, decoherence often limits the fidelity of state-of-the-art gates. Consequently, to build useful quantum hardware, we aim to increase system coherence and decrease gate times as much as possible.

The speed of quantum logic gates is generally limited by effects that become significant as gate times approach relevant system timescales. As a primary example, leakage to non-computational states becomes significant when gate times approach the timescale set by the

qubit anharmonicity [10, 11]. This example is especially relevant for transmon qubits [3, 12], for which low anharmonicities of typically  $|\alpha|/2\pi \sim 200$  MHz limit gate times to  $(|\alpha|/2\pi)^{-1} \sim 5$  ns [13, 14]. As another example, linear drives [15] for gates with durations approaching the qubit Larmor period ( $t_g/\tau_L \rightarrow 1$ ) give rise to significant undesirable counter-rotating dynamics, resulting from the breakdown of the rotating-wave approximation (RWA) [16–19]. These effects are typically negligible for transmons due to their high transition frequency ( $t_g/\tau_L \gtrsim 5 \text{ ns} \cdot 4 \text{ GHz} = 20$ ).

Both the intrinsic control limitations and coherence properties of a particular qubit are dictated by its Hamiltonian. The interplay between qubit anharmonicity, sensitivity to noise, and circuit simplicity for superconducting qubits has been elucidated over the past several decades [2, 20–27], leading to the transmon as the current workhorse superconducting qubit. However, the limitations imposed by its low anharmonicity and unprotected computational states [28] have motivated further investigation of circuits with more favorable coherence and control properties. The fluxonium [25] is one such qubit, featuring a transition frequency typically less than 1 GHz, with state-of-the-art coherence times and single- and two-qubit gate fidelities [29–33]. One beneficial property of the fluxonium is its high anharmonicity, typically several gigahertz, when operated at a flux bias of a half magnetic flux quantum  $\Phi_0/2$ . This property mitigates leakage during fast single-qubit gates, enabling the exploration of new dominant error channels and strategies to mitigate them. In particular, fast, res-

\* These authors contributed equally; [rower@mit.edu](mailto:rower@mit.edu)

† These authors contributed equally; Present address: *Atlantic Quantum, Cambridge, MA 02139*

‡ Present address: *HRL Laboratories, Malibu, CA 90265*

§ Present address: *Atlantic Quantum, Cambridge, MA 02139*

¶ [william.oliver@mit.edu](mailto:william.oliver@mit.edu)

onant control of fluxonium naturally places one in the regime  $t_g/\tau_L \lesssim 5 \text{ ns} \cdot 1 \text{ GHz} = 5$ , where errors due to counter-rotating effects start to become severe.

In this work, we explore fast single-qubit gates based on the resonant control of a fluxonium qubit in the regime of few-cycle pulses ( $1 \lesssim t_g/\tau_L \lesssim 5$ ), where errors from counter-rotating dynamics are significant. We develop two complementary strategies for mitigating these errors. Our first strategy takes inspiration from circularly polarized free-space electromagnetic fields and realizes tunable-polarization drives [34] with simultaneous charge and flux control. We demonstrate the tunability of drive polarization and the calibration of co-rotating drives for gates. Our second strategy, enabling fidelities exceeding 99.997% with only a linear drive, involves leveraging the time-periodicity of the counter-rotating fields to regularize their contributions to all pulses [35]. This approach, hereafter referred to as commensurate pulses, eliminates the coherent error channel posed by counter-rotating effects with no additional calibration overhead and can be implemented straightforwardly to mitigate these effects in any platform where fast resonant control is desired. We utilized both approaches to implement single-qubit gates, exploring different drive schemes—charge, flux, and circularly polarized drives—and the resulting fidelity dependence on the gate duration. Finally, we developed an error budget for our gates and investigated their stability, finding that our best gates were coherence limited, and the performance remained stable (error per gate fluctuations  $\lesssim 1.13 \times 10^{-5}$ ) for the entire measurement duration of 34 hours after an initial calibration.

## II. DEVICE AND THEORY

In this section, we detail the device, our two complementary protocols for mitigating counter-rotating errors for fast gates, and our single-qubit gate implementation.

### A. Fluxonium Device

Our device comprises a two-dimensional differential fluxonium qubit capacitively coupled to a charge line and inductively coupled to a flux line as shown in Fig. 1(a). Modeling just the fluxonium qubit and the two drive lines, our device obeys the system Hamiltonian

$$\hat{H} = \hat{H}_0 + \hbar\Omega_c \cos(\omega_d t) \hat{n} + \hbar\Omega_f \cos(\omega_d t - \Delta\varphi) \hat{\phi}, \quad (1)$$

where  $\hat{H}_0$  is the bare fluxonium Hamiltonian

$$\hat{H}_0 = 4E_C \hat{n}^2 + \frac{1}{2} E_L \hat{\phi}^2 - E_J \cos(\hat{\phi} - \phi_{dc}). \quad (2)$$

This Hamiltonian is written in the lab frame, where  $\Omega_c$  ( $\Omega_f$ ) describes the amplitude of a cosinusoidal charge (flux) drive with frequency  $\omega_d$  and phase difference  $\Delta\varphi$  between the two drives. In the fluxonium Hamiltonian,  $\hat{n}$

and  $\hat{\phi}$  represent the charge and phase operators,  $E_C/h = 1.30 \text{ GHz}$ ,  $E_L/h = 0.59 \text{ GHz}$ , and  $E_J/h = 5.71 \text{ GHz}$  are the charging-, inductive-, and Josephson energy, respectively, and  $\phi_{dc}$  is a phase offset resulting from a static external magnetic flux  $\Phi_{dc}/\Phi_0 = \phi_{dc}/2\pi$  supplied by a superconducting coil inductively coupled to the fluxonium loop. The sample qubit was a subsystem of a device comprising two fluxonium qubits with a capacitively-coupled transmon coupler (refer to device A, fluxonium 2 of Ref. [32]). We note that the linear flux drive arises from the allocation of time-dependent flux inside the inductor term, which has recently been theoretically and experimentally verified [36, 37].

Our experiments were performed at  $\Phi_{dc} = 0.5\Phi_0$ , where the qubit had a frequency  $\omega_{01}/2\pi \approx 243 \text{ MHz}$  (Larmor period  $\tau_L \approx 4.1 \text{ ns}$ ) and coherence times generally between  $200 \mu\text{s} \lesssim T_1, T_{2E} \lesssim 500 \mu\text{s}$ . Dispersive readout was performed with a capacitively-coupled resonator at frequency  $\omega_r/2\pi = 7.08 \text{ GHz}$ , with linewidth  $\kappa/2\pi \approx 1.5 \text{ MHz}$  and dispersive shift  $\chi/2\pi \approx 1 \text{ MHz}$  [38]. We herald the desired initial state with a preceding projective measurement, with a buffer time of  $2 \mu\text{s}$  before applying qubit pulses to avoid photon-shot-noise dephasing. All charge and flux control pulses were directly synthesized on a high-bandwidth arbitrary waveform generator (see Appendix A for details).

We emphasize the relevance of fluxonium qubits for our experiments exploring counter-rotating dynamics, as their typically low qubit frequency and high anharmonicity cause counter-rotating effects to manifest before leakage into non-computational states is observed when performing Rabi-based single-qubit gates.

### B. Circularly Polarized Driving

Here, we detail the ability to tune qubit drive polarization by controlling the relative phase  $\Delta\varphi$  of simultaneous charge and flux drives [Fig. 1(b)]. Truncating to the ground and first excited state manifold of the system Hamiltonian Eq. (1) and considering charge and flux drives of the same strength ( $\Omega_c |\langle 0 | \hat{n} | 1 \rangle| = \Omega_f |\langle 0 | \hat{\phi} | 1 \rangle| \equiv \Omega/2$ ), the two-level Hamiltonian, with  $\hat{H} |0\rangle = 0$ , takes the form

$$\begin{aligned} \frac{\hat{H}}{\hbar} &= \omega_{01} |1\rangle \langle 1| \\ &\quad - i \frac{\Omega}{4} \cos(\omega_d t) (|0\rangle \langle 1| - |1\rangle \langle 0|) \\ &\quad + \frac{\Omega}{4} \cos(\omega_d t - \Delta\varphi) (|0\rangle \langle 1| + |1\rangle \langle 0|). \end{aligned}$$

From the above equation, we see that the two drive terms act along orthogonal axes of the Bloch sphere in the lab frame. This is a consequence of the canonically conjugate nature of the charge and flux operators, and it enables the effective field polarization to be tuned by the relative phase of the charge and flux drives. This may be

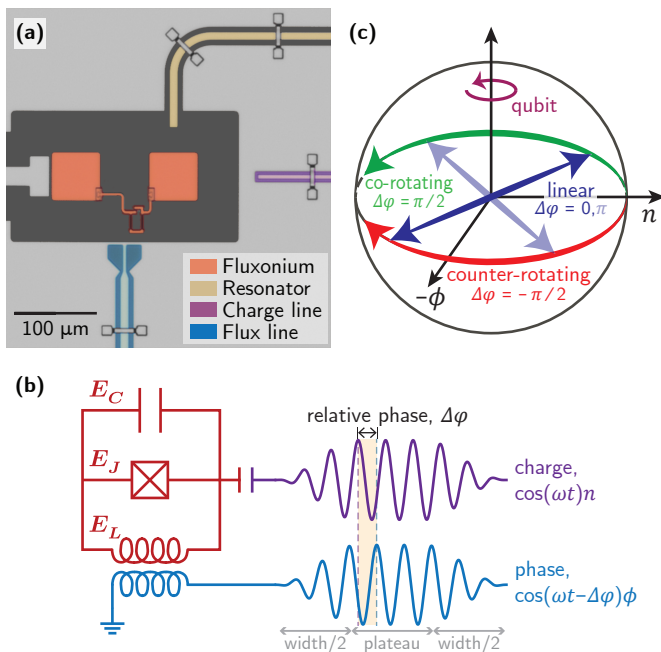


FIG. 1. **Device and concept.** (a) False-colored optical micrograph of the fluxonium qubit (orange) with a coupled charge (purple) and flux line (blue). (b) Diagram illustrating how all drives are performed in this experiment. All drives comprise a phase-sensitive linear combination of a charge and flux drive, parameterized by a cosine-shaped rise-fall and a flat top. (c) Bloch sphere representation of a qubit with the trajectory of various drive polarization vectors drawn. A co-rotating (green) drive has a polarization vector rotating with the same orientation as the qubit, a counter-rotating (red) drive has a polarization vector rotating in the opposite direction as the qubit, and a linear (blue) drive has a polarization vector which traces out a line.

contrasted with the polarization of free-space electromagnetic fields, where polarization is defined by the relation of real-space field components.

**Linear drives.** Setting the relative phase to  $\Delta\varphi = 0$  ( $\pi$ ) [Fig. 1(c), blue] yields a linearly polarized drive with drive operator  $\hat{n} + \hat{\phi}$  ( $\hat{n} - \hat{\phi}$ ). One can also trivially generate linear drives by applying an individual charge or flux drive (oscillating only along the  $n$  or  $\phi$  axes respectively).

**Co-rotating drives.** With  $\Delta\varphi = \pi/2$  [Fig. 1(c) green], the net drive field instead travels along the equator of the Bloch sphere in the same direction as the qubit Larmor precession [Fig. 1(c) purple]. Performing a rotating-frame transformation [39] with frequency  $\omega_d$  co-rotating with the qubit results in a time-independent Hamiltonian without the RWA (details in Appendix B),

$$\frac{\hat{H}_{\text{co}}}{\hbar} = (\omega_{01} - \omega_d) |1\rangle \langle 1| - i \frac{\Omega}{2} (|0\rangle \langle 1| - |1\rangle \langle 0|). \quad (3)$$

**Counter-rotating drives.** Alternatively, for  $\Delta\varphi = -\pi/2$  [Fig. 1(c), red], the drive field travels along the equator but opposite to the qubit Larmor precession.

In a frame counter-rotating relative to the qubit at frequency  $\omega_d$ , we likewise find a time-independent Hamiltonian without making the RWA,

$$\frac{\hat{H}_{\text{counter}}}{\hbar} = (\omega_{01} + \omega_d) |1\rangle \langle 1| - i \frac{\Omega}{2} (|0\rangle \langle 1| - |1\rangle \langle 0|). \quad (4)$$

We emphasize that the ability to realize circularly polarized electromagnetic fields with superconducting qubit drives ultimately relies on the charge and flux drive operators being linearly independent and on the equatorial plane of the qubit Bloch sphere.

### C. Commensurate Pulses: Regularizing Coherent Errors from Counter-Rotating Terms

In this section, we detail a complementary method for mitigating counter-rotating errors even when employing a linear drive. For clarity, we explore resonant drives in this section, but provide analysis for the general case of off-resonant drives in Appendix C. In contrast to the implementation of co-rotating drives, this method relies solely on restricting pulse application times according to the qubit frequency, i.e., no additional calibration overhead is required relative to conventional Rabi gates. In addition to regularizing counter-rotating effects, this approach also regularizes other sources of error, e.g., AC Stark shifts or transients which depend on pulse profiles, and can be straightforwardly implemented in parallel with typical gate calibration methods.

We introduce this method by considering a qubit subjected to a resonant, linearly polarized pulse of duration  $t_g$  applied at a start time  $t_0$

$$\frac{\hat{H}}{\hbar} = \omega_{01} |1\rangle \langle 1| + \Omega(t-t_0) \cos(\omega_{01}t + \varphi) (|0\rangle \langle 1| + |1\rangle \langle 0|), \quad (5)$$

where  $\Omega(t' = t - t_0)$  denotes the envelope of the pulse such that  $\Omega(t') = 0$  for  $t' < 0$  and  $t' > t_g$ . Rewriting the Hamiltonian in terms of  $t'$  and in a frame co-rotating with the qubit at frequency  $\omega_{01}$ ,

$$\frac{\hat{H}}{\hbar} = \frac{e^{i\varphi}\Omega(t')}{2} \left[ 1 + e^{-2i(\omega_{01}(t'+t_0)+\varphi)} \right] |0\rangle \langle 1| + \text{h.c.}, \quad (6)$$

and the time-evolution operator generated by the pulse is given by

$$\hat{U}(t' = t_g, t' = 0) = \exp \left[ -\frac{i}{\hbar} \int_0^{t_g} \hat{H}(t', t_0) dt' \right]. \quad (7)$$

By inspecting the counter-rotating field—the second term in the square brackets of Eq. (6)—we can interpret the pulse start time  $t_0$  as effectively setting a phase offset of the counter-rotating field. When working within the RWA (neglecting the counter-rotating term), the rotating-frame Hamiltonian and resulting unitary given

by Eq. (7) become invariant with respect to  $t_0$ . In contrast, when applying strong linear drives with  $1/t_g$  approaching  $\omega_{01}/2\pi$ , the counter-rotating field cannot be neglected and the unitary remains a function of  $t_0$ . In other words, counter-rotating effects cause the qubit rotation to depend on when the pulse is applied [40].

However, noting that this effect is coherent and deterministic, we can make the contribution from counter-rotating fields uniform for all pulses by utilizing their time periodicity. In particular, the exponential in Eq. (6) has a period of  $\tau = \pi/\omega_{01} = \tau_L/2$ . So, restricting the times at which we apply pulses to  $t_0 = n\tau_L/2 + \delta t_0$  with integer  $n$  and arbitrary constant time-offset  $\delta t_0$  leads to the same unitary dynamics for every pulse of a fixed  $\varphi$ . We set  $\delta t_0 = 0$  as this time offset is equivalent to an absolute carrier-phase offset  $\varphi \rightarrow \varphi - \omega_{01}\delta t_0$ . As a result of regularizing the pulse unitary, any calibration that can correct for a systematic rotation error automatically mitigates the counter-rotating contribution. We refer to gates performed with this approach as commensurate, since pulses are locked to a lattice defined by  $\tau_L/2$ .

We refer to gates not following this restriction as incommensurate and highlight their susceptibility to the coherent error generated by the non-uniform sampling of counter-rotating fields for pulses applied at different times. We further note that when performing pulse sequences composed of a large number of incommensurate pulses, each pulse contributes a different counter-rotating error, reducing fidelity and rendering a global shift of the carrier phase  $\varphi$  to all pulses indiscernable. In contrast, a pulse sequence employing commensurate pulses will generally be sensitive to such a global offset in  $\varphi$ .

To form a gate set with  $X$  and  $Y$  rotations (i.e. with phases  $\varphi \in \{0, \pi/2\}$ ), we can regularize the counter-rotating dynamics for both phases simultaneously by applying  $X$  gates at times  $t_0^X = n\tau_L/2$  and  $Y$  gates at  $t_0^Y = (n + 1/2)\tau_L/2$  [41]. Pragmatically, this can be implemented by defining  $X$  gates to have a duration that is a multiple of  $\tau_L/2$  and forming  $Y$  gates by padding  $X$  gates before and after with duration  $\tau_L/4$  identity gates. These identity gates can be compiled away for consecutive  $Y$  gates to reduce the total sequence duration. In practice, we found the benefit from this compilation to be minimal and did not utilize it for data presented in this paper.

To conclude this subsection, we highlight that commensurate gates offer the ability to regularize and thereby eliminate coherent errors from the counter-rotating component of strong linear drives with no additional calibration overhead. This stands in contrast to co-rotating drives, which natively do not include a counter-rotating component but require extra calibration. In practice, we still found that co-rotating gates with durations approaching  $\tau_L$  benefited from adhering to the commensurate condition—we attribute this to the regularization of AC Stark shifts arising from the off-resonant driving of transitions beyond  $0 - 1$ . The AC Stark shift magnitude is dependent on when co-rotating

pulses are applied due to the varying relative value of charge and flux drive components, which couple the non-target levels with different matrix elements. This effect also grows with increasing drive strength, and its mitigation highlights another distinct benefit of commensurate gates. We further emphasize that this approach does not rely on any specific details of the qubit. In other words, this approach can be applied to mitigate counter-rotating effects in any platform where strong linear drives are desired. The small price to pay for applying commensurate gates is in coherence—by requiring  $X$  and  $Y$  gates to be applied at times belonging to lattices shifted by  $\tau_L/4$  relative to each other, the target qubit accrues decoherence during the  $\tau_L/4$  waiting times between applying  $X$  then  $Y$  or  $Y$  then  $X$  gates. For our qubit, this amounted to 2.05 ns for every such occasion.

## D. Single-Qubit Gates

In this subsection, we detail the implementation of our single-qubit gates. We performed gates with three driving schemes: circularly polarized, purely charge [31, 32], and purely flux [42].

**Calibrating the  $\pi/2$  pulse.** For all drive schemes, a  $\pi/2$  rotation was explicitly calibrated with Rabi driving and pulse train techniques. Circularly polarized drives underwent additional calibration steps to ensure (1) equal drive strengths between the two drives, (2) a relative drive phase corresponding to a co-rotating circular polarization, and (3) simultaneity of the charge and flux pulse arrivals at the qubit. Following the commensurate restriction required no additional calibration relative to conventional Rabi gates. We include full details on the pulse calibration in Appendix D.

**Forming a gate set.** With a fully calibrated  $\pi/2$  rotation, we defined our  $X$  ( $Y$ ) gate as having no phase shift ( $90^\circ$  phase shift) of the carrier.  $\pi$ -pulses were implemented by playing two  $\pi/2$ -pulses back to back, and  $Z$  gates were implemented as virtual- $Z$  gates [43]. All microwave pulses used a pure-cosine envelope, with a 0.1 ns gap between adjacent pulses.

**Benchmarking and gate decomposition.** Both standard and interleaved Clifford randomized benchmarking were performed to assess the quality of our gates [44, 45]. We generated the single-qubit Clifford group with the gate set  $\mathcal{G} = \{I, \pm X_{\pi/2}, \pm Y_{\pi/2}\}$ , which yields on average  $53/24 \approx 2.208$  non-identity gates per Clifford. We used this decomposition as it comprises the native gates in our experiment and allows direct comparison with other recent works [14, 46] demonstrating state-of-the-art single-qubit gates. All fidelities were reported with uncertainties representing the standard error of the mean.

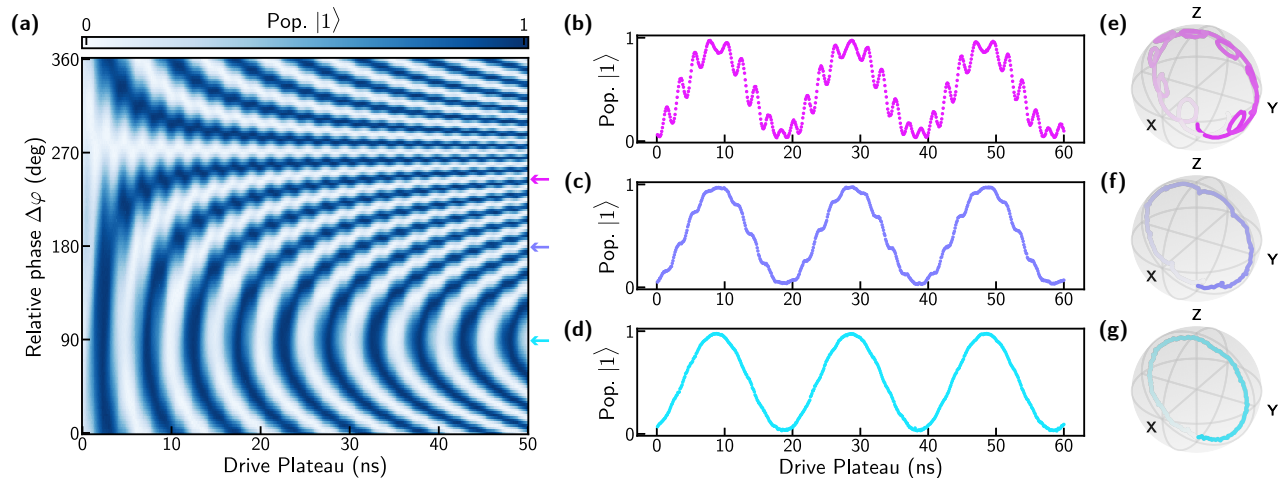


FIG. 2. **Rabi oscillations with tunable drive polarization.** (a) Time-domain Rabi oscillations as the relative phase between the charge and flux drives is varied. The relative strength of the individual charge and flux drives were calibrated to be equal, and kept constant throughout the plot. All oscillations use a 1 ns rise-fall time. (b-d) Similar data taken for three different polarizations, calibrated to each have the same Rabi frequency, all using a 2.5 ns rise-fall time. (b) Nearly completely counter-rotating ( $\Delta\varphi = 245^\circ$ ) Rabi oscillations of the fluxonium qubit. The counter-rotating oscillations are visible on top of the slower co-rotating oscillation. (c) Linearly polarized drive ( $\Delta\varphi = 180^\circ$ ) with equal contributions from charge and flux. (d) Completely co-rotating drive ( $\Delta\varphi = 90^\circ$ ) illustrating elimination of counter-rotating effects. The remaining small distortions are a result of the fast rise-time of the pulse. (e-f) Bloch-sphere trajectories of the corresponding oscillations (truncated to the first Rabi flop) of the data in (b-d). Opaque color corresponds to the start time, and transparent corresponds to the end time.

### III. EXPERIMENT

In this section, we describe our three main results: (1) the demonstration of tunable-polarization drives, (2) the mitigation of counter-rotating errors for linearly polarized drives with commensurate gates, and (3) the optimization of gate duration for different drive schemes.

#### A. Arbitrarily Polarized Drives

As our first experiment, we demonstrated the generation of arbitrarily polarized microwave drives. To ensure equal drive strengths for the charge and flux components, we first calibrated the charge and flux drive amplitudes to individually produce the same Rabi frequency. Then, time-domain Rabi oscillations were measured with the relative phase  $\Delta\varphi$  of the two simultaneous drives swept between  $0^\circ$  and  $360^\circ$  [Fig. 2(a)]. In this plot, the drive is shown to continuously vary between a completely co-rotating drive ( $\Delta\varphi = 90^\circ$ ) and a completely counter-rotating drive ( $\Delta\varphi = 270^\circ$ ). In between, at  $\Delta\varphi = 0^\circ$  and  $\Delta\varphi = 180^\circ$ , the drive is completely linearly polarized, but along a diagonal axis in the Bloch sphere equatorial plane [Fig. 1(c), blue arrows]. The counter-rotating dynamics are visibly apparent as fast oscillations on top of the slower Rabi flopping away from  $\Delta\varphi = 90^\circ$ . The Rabi frequency of the simultaneous drive (within the RWA) depends on the relative phase, and is given by Eq. B6.

To fairly compare the dynamics for Rabi drives of dif-

ferent polarizations, we then separately calibrated Rabi drives of the same strength for a mostly counter-rotating drive [Fig. 2(b)], a linear drive with equal charge and flux components [Fig. 2(c)], and a co-rotating drive [Fig. 2(d)]. The associated Bloch sphere trajectories measured with state tomography are shown in panels Fig. 2(e-g) respectively.

In both simulation and experiment, we found that a slow rise and fall of the pulse envelope could dampen the effects of the counter-rotating terms by allowing the Hamiltonian to change adiabatically relative to the counter-rotating drive contribution [18]. Here, to magnify the counter-rotating oscillations, we used pulses with a total rise and fall time of 1 ns for the data in Fig. 2(a) and 2.5 ns for the data in Fig. 2(b-g).

The apparent tuning of the counter-rotating drive strength as a function of  $\Delta\varphi$  confirms both our circuit QED analogy to optical polarization and that our two drive lines truly couple to the qubit through canonically conjugate operators; if the two drives coupled through the same operator, the Rabi frequency would still be observed to tune from a local maximum to zero as in Fig. 2(a), but no increase in counter-rotating dynamics would be observed near  $\Delta\varphi = 270^\circ$ . Our technique also simplifies further research involving counter-rotating dynamics by enabling direct access to purely counter-rotating drives.

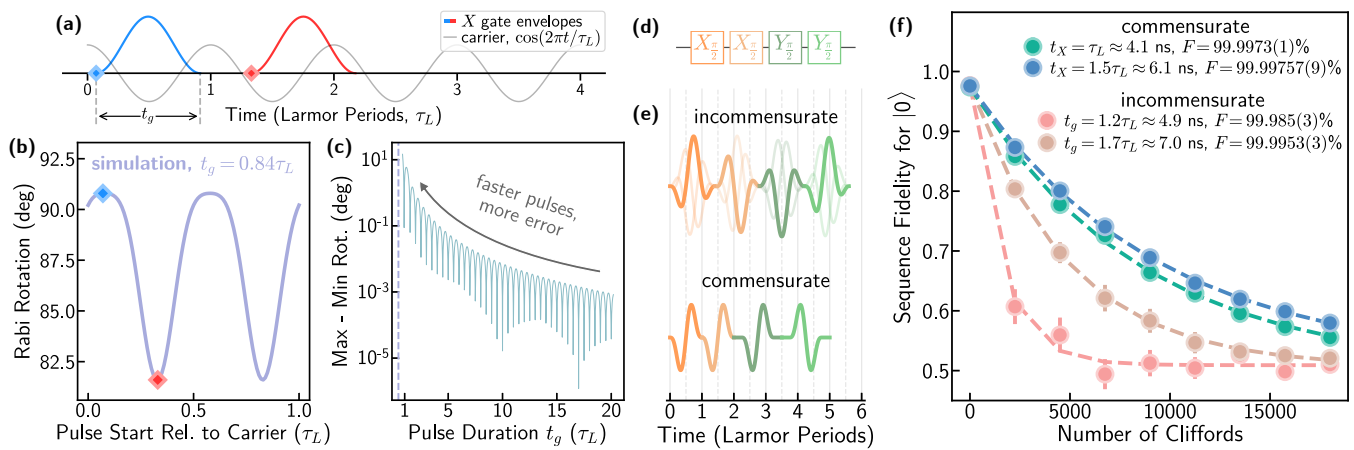


**FIG. 3. Commensurate gates: alleviating counter-rotating errors for linear drives.** (a) Time-domain depiction of two resonant linearly polarized  $X$ -pulse envelopes (red and blue), starting at different times relative to the carrier ( $\cos(2\pi t/\tau_L)$ , grey), where  $\tau_L$  is the qubit Larmor period. (b) Rabi rotation angle (polar angle of the Bloch vector) of an ideal two-level system starting in the ground state subject to an  $X$  pulse of duration  $t_g = 0.84\tau_L$  as a function of the pulse start time modulo  $\tau_L$ . The rotations from the pulses in (a) are highlighted as points on the plot. The qubit rotation depends strongly on the pulse start time due to the time dependence of the counter-rotating drive component. (c) Rotation angle range versus pulse duration, showing the divergence of this effect for short pulse times. The dotted line represents the pulse duration used in (b). (d) Example single-qubit circuit. (e) Cartoon waveforms for two different implementations of the circuit drawn in (d). Top: incommensurate pulses ( $t_g = 1.2\tau_L$ ), which suffer from the coherent error channel depicted in panel (b). Bottom: commensurate pulses ( $t_X = \tau_L$ ,  $t_Y = 1.5\tau_L$ ), which regularize the counter-rotating fields during each pulse. This turns the coherent errors which were previously different for each pulse into a systematic coherent rotation which is corrected for automatically in our other calibrations. For the reasons described in Section II C, commensurate  $Y$  pulses require  $\tau_L/4$  identity-gate padding before and after each pulse. (f) Clifford randomized benchmarking (RB) of single-qubit gates performed with flux pulses, comparing commensurate and incommensurate implementations. All curves were averaged over 40 random seeds. We include data from two incommensurate pulse durations ( $t_g = 1.2\tau_L \approx 4.92$  ns and  $t_g = 1.7\tau_L \approx 6.97$  ns), and two commensurate implementations ( $t_X = 1.0\tau_L \approx 4.1$  ns and  $t_X = 1.5\tau_L \approx 6.15$  ns). At these gates times, we see a significant increase in fidelity by using commensurate pulses. This highlights the ability to mitigate coherent errors from counter-rotating terms for strong linear drives by adopting straightforward pulse-timing constraints.

## B. Commensurate Gates

In this subsection, we highlight the coherent error channel posed by the non-uniform sampling of counter-rotating fields for resonant pulses applied at different times relative to the carrier phase and the mitigation of this error channel with commensurate gates.

To establish this error channel, we simulated a two-level system subjected to an  $X$  pulse applied at different start times Fig. 3(a). We plot the the polar angle traversal of the ground state Bloch vector after application of the pulse (with duration  $t_g = 0.84\tau_L$ ) as a function of the pulse start time in Fig. 3(b). Shifting the pulse start by  $0.5\tau_L$  corresponds to a  $\pi$  phase shift of the carrier at the start of the pulse (leading to a rotation of the same amount, but in the opposite direction), resulting in a  $0.5\tau_L$  periodicity of the effective rotation angle. We then simulated this effect as a function of the pulse duration [Fig. 3(c)], plotting the rotation range as a proxy for the coherent error. It is apparent that, as pulse durations approach  $\tau_L$ , this error channel grows significantly.

In order to mitigate this error channel, we adopted the commensurate approach detailed in Section II C. This

approach entailed applying pulses at times constrained to a lattice of spacing  $\tau_L/2$  for  $X$  gates (and the corresponding lattice shifted by  $\tau_L/4$  for  $Y$  gates, which we implemented by padding  $Y$  gates before and after with  $\tau_L/4$  wait times such that  $Y$  gates had durations  $\tau_L/2$  longer than those of  $X$  gates). Intuitively, this amounts to sampling only a single point in Fig. 3(b). We draw a simple single-qubit circuit and waveforms implementing it in Fig. 3(d,e) with both incommensurate pulses of duration  $t_g = 1.2\tau_L$  and commensurate pulses of duration  $t_X = \tau_L$  ( $t_Y = 1.5\tau_L$ ).

We implemented both commensurate and incommensurate single-qubit gates and characterized their performance with Clifford randomized benchmarking [Fig. 3(f)]. For commensurate gates, we additionally optimized the absolute carrier phase offset, which effectively determines the shape of the regularized waveform. The dependence of the fidelity on this phase was larger for shorter gates, with a most extreme variation of  $5 \times 10^{-5}$ . We attribute this dependence to the compensation of, e.g., transients or a slight offset of the qubit flux bias, which would affect the qubit trajectory through the 0-1 avoided crossing. Notably, commensurate gates with durations as low as  $\tau_L$  were characterized by fidelities well in

excess of 99.997%, in contrast to incommensurate pulses at similar times which were characterized by fidelities as low as 99.985%. As expected, the benefit from commensurate pulses was more significant for faster gates.

### C. Linear and Circular Gate Characterization

As a final experiment, we empirically optimized the duration of our commensurate gates by measuring the average single-qubit gate fidelity as a function of the gate duration for three driving schemes: charge, flux, and co-rotating drives [Fig. 4(a)]. Coherence bounds were calculated using the average gate time  $t_g = (t_X + t_Y)/2 = t_X + \tau_L/4$ . We found all drive schemes were optimal near  $t_X = 2\tau_L \approx 8.2$  ns, with fidelities  $> 99.994\%$  for charge,  $> 99.996\%$  for circular co-rotating, and  $> 99.997\%$  for flux drives. Linear flux (charge) drives resulted in our best (worst) gates, with circular drives performing better than charge but worse than flux. We separately performed interleaved randomized benchmarking using the  $t_X = 2\tau_L$  flux pulses for each gate in our gate set [Fig. 4(b)]. We further explored the distribution of errors and gate stability in Appendix F. We present additional data comparing incommensurate linear and circular gates in Appendix G, demonstrating that circular drives can benefit incommensurate gates, but do not outperform flux-driven commensurate gates.

## IV. OUTLOOK

The effect of counter-rotating dynamics on gate operations has long been an understudied aspect of Rabi-oscillation-based gates. With the growing popularity of fluxonium and other low-frequency qubits as well as the ongoing development of control strategies to mitigate other dominant error channels [14], counter-rotating effects have become increasingly relevant for calibrating fast, high-fidelity microwave gates. We introduced and demonstrated two complementary approaches for mitigating these effects.

Our first protocol uses independently controlled linear charge and flux drives, representing two independent quadratures in circuit QED. This control enables the ability to change the polarization angle of the total effective drive, giving a controllable means to study counter-rotating dynamics and the trade-offs between different linear drives. Using such control, we demonstrated the ability to create a circularly polarized drive—natively lacking a counter-rotating component, independent of the drive amplitude—for use in gates.

Our second protocol, commensurate pulses, leverages the coherent and time-periodic nature of counter-rotating fields to regularize their contributions to all control pulses, thereby eliminating the counter-rotating error channel for linear drives. This protocol relies on the application of gates at periodically discrete times deter-

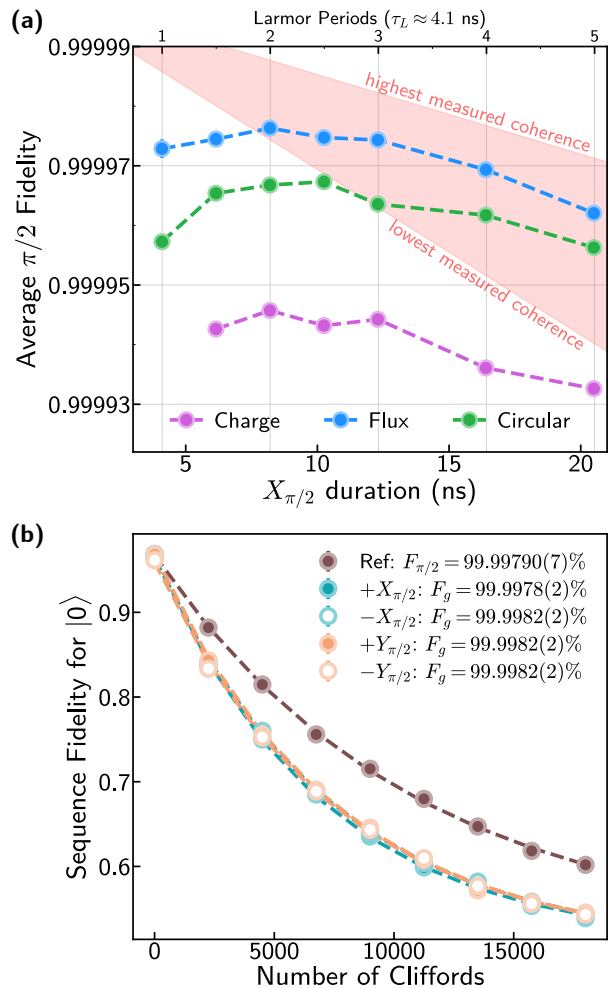


FIG. 4. **Commensurate single-qubit gates with linear and circularly polarized drives.** (a) Gate fidelity measured with Clifford randomized benchmarking as a function of the  $\pi/2$ -pulse width for a pure charge drive (purple), pure flux drive (blue), and a co-rotating circularly polarized drive (green). In order to mitigate the effect of coherence fluctuations, data was collected over a span of two weeks with intermittent breaks taken when the qubit coherence fluctuated to low values. The lowest and highest measured coherences during this window ( $300 \mu\text{s} \lesssim T_1 \lesssim 500 \mu\text{s}$ ,  $200 \mu\text{s} \lesssim T_{2E} \lesssim 500 \mu\text{s}$ ) were used to calculate fidelity bounds (red). (b) Clifford interleaved randomized benchmarking for a calibrated linearly polarized flux drive with an  $X_{\pi/2}$  duration of  $t_X = 2\tau_L$ . The reference trace has an average single-qubit gate error of  $(2.10 \pm 0.07) \times 10^{-5}$ . All randomized benchmarking traces were averaged over 25 random seeds.

mined by the qubit Larmor period, is platform independent, and requires no additional calibration overhead for Rabi-based gates. We established the efficacy of this protocol for gates as short as one Larmor period, finding almost an order of magnitude improvement in fidelity over incommensurate pulses of a similar duration.

We note that our commensurate pulse technique shares close resemblance with those used for Landau-Zener-

based single-qubit gates [41, 47]. In both schemes, the exact specification of the waveform, including its timing, is crucial for the fidelity of the gate. However, these gates are often viewed from a different perspective; commensurate pulses are readily modeled in a rotating frame, whereas Landau-Zener gates are not. In the lab frame, the natural qubit precession supports  $Z_{\phi(t)}$  gates by idling for a time  $t$ . Identity gates that are not exact multiples of the Larmor period must then be performed by modulating the qubit frequency [48]. Likewise, identity gates of arbitrary duration cannot be performed in the rotating frame without relaxing the commensurate pulse conditions, and  $Z$  gates are implemented via a combination of idling and phase shifting the next drive pulse so that it is once again commensurate. The main advantage of commensurate pulses is the ability to use a stable underlying carrier frequency in hardware (e.g. with a dedicated RF source). With this in place, errors in envelope timing only translate into small errors in the polar rotation angle [Fig. 3(c)], whereas without, errors in timing freely rotate the equatorial axis of the gate. This advantage is more pronounced when the qubit frequency is higher. While the language to describe these operations is often different, both pairs of gates rely on the same underlying physics of the natural qubit precession to perform  $I$ - and  $Z$ -gates.

We demonstrated state-of-the-art single-qubit gates with three separate drive schemes on the same qubit (pure charge, pure flux, and circularly polarized), and found that flux pulses performed the best. We attribute this to extra decoherence from system heating associated with the charge drive (see Appendix F) and the matrix element structure of the fluxonium at half-flux (featuring larger charge matrix elements for transitions to states outside the computational subspace). We hypothesize that, if leakage transitions and heating were mitigated for charge drives, circularly polarized drives may potentially benefit Rabi-based gates for even more aggressive gate times. Furthermore, a circularly polarized drive remains an attractive tool when optimizing single-qubit gates in even lower-frequency qubits [41, 47, 49, 50] and for other low-frequency microwave interactions such as cross-resonance [51], iSWAP [33], or bSWAP gates [52].

We expect commensurate pulses, being platform-independent and requiring no additional calibration overhead, to benefit any platform where fast, resonant control is desired and counter-rotating dynamics are problematic. Although our demonstration only included one qubit, we note the straightforward extension of commensurate pulses to a multi-qubit processor based on resonant single-qubit control. Each qubit  $i$  will have an associated Larmor period  $\tau_L^i$ , and so control pulses for each qubit will follow their individual lattices as defined in II C. Any multi-qubit gate then simply needs to allocate a requisite number of Larmor periods from each qubit to accommodate the duration of the added gate. Aside from the short idling times this requires, the compilation of commensurate pulses with multiple qubits needs no

other special consideration.

*Note:* While preparing this manuscript, we became aware of a related work [53]

## ACKNOWLEDGMENTS

We gratefully acknowledge insightful conversations with Réouven Assouly, Samuel Alipour-Fard, David Newsome, Lamia Ateshian, Amir Karamlou, Youngkyu Sung, and Agustin Di Paolo. This research was funded in part by the U.S. Army Research Office under Award No. W911NF-23-1-0045; in part by the U.S. Department of Energy, Office of Science, National Quantum Information Science Research Centers, Co-design Center for Quantum Advantage (C2QA) under contract number DE-SC0012704; and in part under Air Force Contract No. FA8702-15-D-0001. M.H., P.M.H., and I.T.R. are supported by an appointment to the Intelligence Community Postdoctoral Research Fellowship Program at MIT administered by Oak Ridge Institute for Science and Education (ORISE) through an interagency agreement between the U.S. Department of Energy and the Office of the Director of National Intelligence (ODNI). D.A.R. gratefully acknowledges support from the NSF (award DMR-1747426). Any opinions, findings, conclusions or recommendations expressed in this material are those of the author(s) and do not necessarily reflect the views of the US Air Force or the US Government.

## Appendix A: Wiring and Control Hardware

All experiments were conducted in a Bluefors XLD600 dilution refrigerator maintaining a base temperature stabilized at  $\sim 22$  mK. Flux biases were provided by a small superconducting solenoid mounted to the lid of the sample package. We specify the equipment used for qubit biasing, control, and readout in Table. I, and detail the experimental wiring in Fig. 5.

TABLE I. Summary of control equipment.

Component	Manufacturer	Model
Dilution Refrigerator	Bluefors	XLD600
RF Source	Rohde and Schwarz	SGS100A
DC Source	QDevil	QDAC I
Control Chassis	Keysight	M9019A
AWG (readout pulses)	Keysight	M3202A
AWG (qubit pulses)	Keysight	M8195A
ADC	Keysight	M3102A

## Appendix B: Circularly Polarized Driving

In this section, we present derivations for the co- and counter-rotating drive Hamiltonians in the fluxonium qubit subspace. We also derive an expression for the Rabi



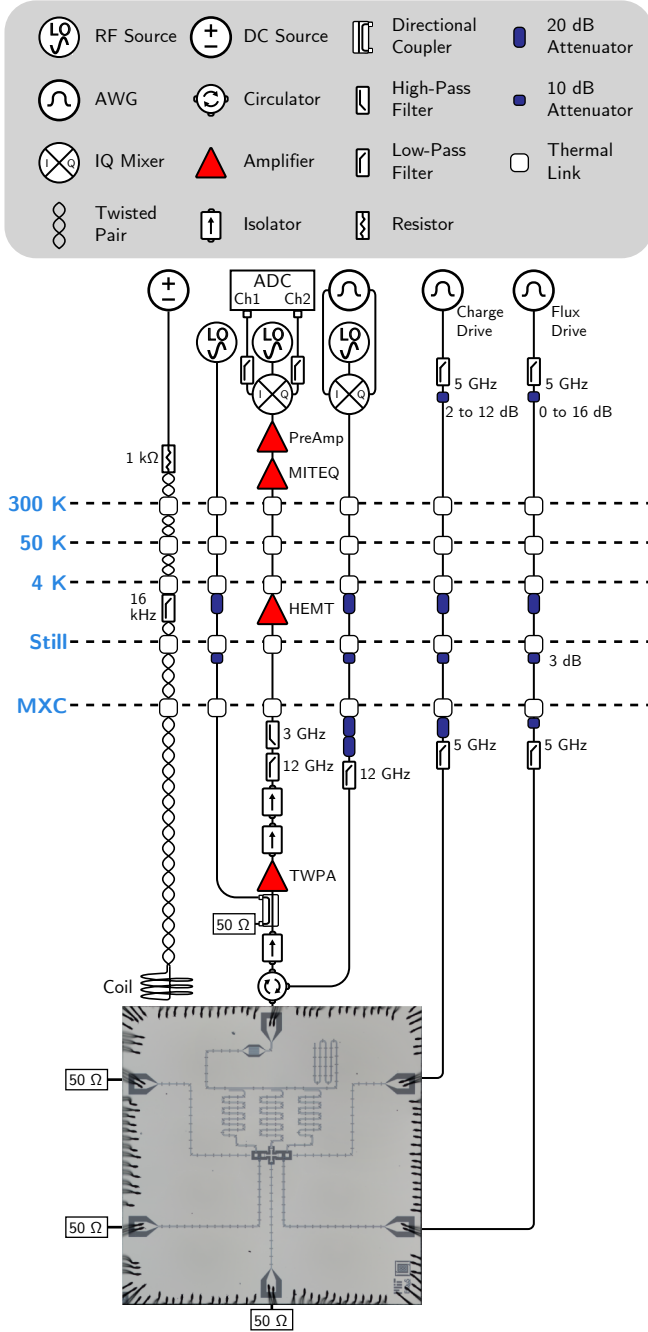


FIG. 5. Wiring schematic of the experimental setup.

frequency (within the RWA) as a function of the relative phase between simultaneous charge and flux drives.

Truncating to the ground and first excited state manifold of the system Hamiltonian Eq. 1, the two-level Hamiltonian terms take the following form

$$\begin{aligned}\hat{H}_0 &\rightarrow \hbar\omega_{01} |1\rangle \langle 1|, \\ \hat{n} &\rightarrow i(|0\rangle \langle 1| - |1\rangle \langle 0|), \\ \hat{\phi} &\rightarrow |0\rangle \langle 1| + |1\rangle \langle 0|.\end{aligned}$$

Considering simultaneous charge and flux drives of the same strength  $\Omega_c \langle 0| \hat{n} |1\rangle = \Omega_f \langle 0| \hat{\phi} |1\rangle \equiv \Omega/2$  then yields the two-level system Hamiltonian

$$\begin{aligned}\frac{\hat{H}}{\hbar} &= \omega_{01} |1\rangle \langle 1| \\ &- i\frac{\Omega}{4} \cos(\omega_d t) (|0\rangle \langle 1| - |1\rangle \langle 0|) \\ &+ \frac{\Omega}{4} \cos(\omega_d t - \Delta\varphi) (|0\rangle \langle 1| + |1\rangle \langle 0|).\end{aligned}$$

### 1. Co-rotating Drive

Applying a rotating frame transformation

$$\hat{H} = \hat{U} \hat{H} \hat{U}^{-1} + i\hbar \frac{\partial \hat{U}}{\partial t} \hat{U}^{-1} \quad (\text{B1})$$

at a frequency  $\omega_d$  co-rotating with the qubit,  $\hat{U}_{\text{rf}}(t) = e^{i\omega_d t |1\rangle \langle 1|}$  gives

$$\begin{aligned}\frac{\hat{H}}{\hbar} &= (\omega_{01} - \omega_d) |1\rangle \langle 1| \\ &- i\frac{\Omega}{4} [1 + ie^{-i\Delta\varphi} + e^{-2i\omega_d t}(1 + ie^{i\Delta\varphi})] |0\rangle \langle 1| + \text{h.c.}\end{aligned} \quad (\text{B2})$$

For  $\Delta\varphi = \pi/2$ , the fast-oscillating terms exactly cancel, and the Hamiltonian simplifies to a qubit with a static drive field (without needing the RWA),

$$\frac{\hat{H}_{\text{co}}}{\hbar} = (\omega_{01} - \omega_d) |1\rangle \langle 1| - i\frac{\Omega}{2} (|0\rangle \langle 1| - |1\rangle \langle 0|). \quad (\text{B3})$$

### 2. Counter-rotating Drive

For  $\Delta\varphi = -\pi/2$ , following a similar procedure with a rotating-frame transformation in the opposite direction,  $\hat{U}_{\text{rf}}(t) = e^{-i\omega_d t |1\rangle \langle 1|}$ , gives

$$\frac{\hat{H}_{\text{counter}}}{\hbar} = (\omega_{01} + \omega_d) |1\rangle \langle 1| - i\frac{\Omega}{2} (|0\rangle \langle 1| - |1\rangle \langle 0|). \quad (\text{B4})$$

### 3. Generalized Rabi Oscillations with Simultaneous Drives of Arbitrary Relative Phase

With resonant drives ( $\omega_d = \omega_{01}$ ), the rotating frame Hamiltonian Eq. (B2) only retains the coupling term

$$\frac{\hat{H}}{\hbar} = -i\frac{\Omega}{4} (1 + ie^{-i\Delta\varphi} + e^{-2i\omega_d t}(1 + ie^{i\Delta\varphi})) |0\rangle \langle 1| + \text{h.c.} \quad (\text{B5})$$

For weak drives ( $\Omega \ll \omega_{01}$ ), we can perform the RWA (discard terms oscillating at  $2\omega_d$ ) and the qubit will display generalized Rabi oscillations at a frequency

$$\tilde{\Omega} = \frac{\Omega}{4} |1 + ie^{-i\Delta\varphi}| \quad (\text{B6})$$

$$= \frac{\Omega}{2} |\cos((\Delta\varphi - \pi/2)/2)| \quad (\text{B7})$$

$$= \frac{\Omega}{2} \sqrt{\frac{1 + \cos(\Delta\varphi - \pi/2)}{2}}. \quad (\text{B8})$$

To determine the relative phase offset of the charge and flux drives, we applied simultaneous drives of the same strength while sweeping the relative phase and fit the observed oscillation frequencies to Eq. (B8).

### Appendix C: Commensurate Condition for Off-Resonant Pulses

In this section, we derive a commensurate condition ensuring the uniformity of the qubit rotation for different pulse start times utilizing an off-resonant drive.

Consider a qubit subjected to a linearly polarized pulse of duration  $t_g$  with carrier frequency  $\omega_d = \omega_{01} + \delta$  applied at a variable start time  $t_0$

$$\frac{\hat{H}}{\hbar} = \omega_{01} |1\rangle \langle 1| + \Omega(t - t_0) \cos(\omega_d t + \varphi) |0\rangle \langle 1| + \text{h.c.} \quad (\text{C1})$$

where  $\Omega(t' = t - t_0)$  denotes the pulse envelope such that  $\Omega(t') = 0$  for  $t' < 0$  and  $t' > t_g$ . Rewriting the Hamiltonian in terms of  $t'$  and performing the standard rotating-frame transformation co-rotating with the qubit at frequency  $\omega_{01}$ , we obtain

$$\frac{\hat{H}}{\hbar} = e^{i(\varphi + \delta t_0)} \frac{\Omega(t')}{2} \left[ e^{i\delta t'} + e^{-i(\omega_\Sigma t' + 2\omega_d t_0 + 2\varphi)} \right] |0\rangle \langle 1| + \text{h.c.} \quad (\text{C2})$$

with  $\omega_\Sigma \equiv \omega_d + \omega_{01}$ . The time-evolution operator generated by the pulse is given by

$$\hat{U}(t' = t_g, t' = 0) = \exp \left[ -\frac{i}{\hbar} \int_0^{t_g} \hat{H}(t', t_0) dt' \right]. \quad (\text{C3})$$

**Monochromatic, resonant drive.** In this case,  $\delta = 0$  and Eq. (C2) reduces to Eq. (6). To regularize the unitary for all pulse start times  $t_0$  of a given  $\varphi$ , we require  $t_0 = n\tau_L/2 + \Delta t_0$  with integer  $n$  and arbitrary constant time-offset  $\Delta t_0$ .

**Monochromatic, off-resonant drive.** In this case,  $\delta \neq 0$ . In contrast to the resonant case, we now have an additional  $t_0$  dependence in the phase prefactor in Eq. (C2) which affects the axis of rotation. However, this prefactor is a constant with respect to the  $t'$  integration of Eq. (C3). To regularize the unitary for all pulse start times  $t_0$ , it suffices to regularize the counter-rotating term with  $t_0 = n\tau_d/2 + \Delta t_0$ , where  $\tau_d = 2\pi/\omega_d$  is the drive period. The axis of rotation can be corrected for with a subsequent  $Z$  rotation.

### Appendix D: Single-Qubit Gate Calibration

All gates in this work were made of  $\pi/2$ -pulses (e.g.  $\pi$ -pulses utilized two sequential  $\pi/2$ -pulses) with cosine envelopes and performed at  $\Phi_{\text{ext}} = 0.5\Phi_0$ , referred to as the “sweet spot.” A pulse starting at time  $t_0$  with duration  $t_g$  was implemented with the waveform  $w(t)$ ,

$$w(t) = A(t) \cos[\omega_{01}t - \delta(t - t_0) + \phi]$$

$$A(t) = \begin{cases} \frac{A_0}{2} (1 - \cos[2\pi \frac{(t-t_0)}{t_g}]), & t_0 \leq t \leq t_0 + t_g \\ 0, & \text{otherwise} \end{cases}$$

where  $\omega_{01}/2\pi$  is the undriven qubit frequency,  $\delta$  is the pulse detuning, and  $\phi$  is the phase of the carrier defining the axis of the qubit rotation.

Before precise gate calibration, we performed rough calibrations of the flux bias, qubit frequency, and a slow ( $\geq 30$  ns) charge  $\pi/2$ -pulse for precise flux bias and frequency calibrations. The following preliminary calibrations were performed before gate tune-up.

1. **Precise flux bias calibration.** Ramsey oscillations were measured with a fixed pulse frequency (slightly detuned below the qubit frequency at the sweet spot) as a function of flux bias. The oscillation frequencies vs flux were fit to a parabola, with a minimum oscillation frequency at the flux sweet spot. For details, we refer to [32].
2. **Single-shot readout calibration.** We collected single-shot voltage measurements with no initialization of the qubit, and trained a Gaussian mixture model on the resulting dataset in the IQ plane.
3. **Precise qubit frequency calibration.** Ramsey oscillations were measured for 10  $\mu\text{s}$  with an applied detuning of  $-800$  kHz and fit with a cosine function. The difference between the fit oscillation frequency and the applied detuning was then used to calculate the precise qubit frequency.

Linear drive gates for a given  $\pi/2$ -pulse duration were calibrated roughly following the procedure of [32], with minor adjustments. We detail the exact procedure below.

1. **Rough  $\pi$ -pulse amplitude calibration.** A train of two Rabi pulses was applied to the qubit while sweeping the amplitude of their cosine envelopes. The resulting population of the excited state was fit with a cosine function, yielding the rough amplitude corresponding to two sequential  $\pi/2$  pulses.
2. **Pulse detuning.** A train of  $\pi/2$  pulses with alternating signs (e.g.  $[X_{\pi/2} + X_{-\pi/2}]^n$ ) was applied while sweeping the number of pulses and a detuning modulation of the envelope of each pulse given by  $e^{-i\delta(t-t_0)}$ , where  $t_0$  was the start time of each pulse. The optimal value of  $\delta$  was chosen such that the oscillation between  $|0\rangle$  and  $|1\rangle$  was minimized. Interestingly, for commensurate gates, we

found that the particular pulse used for this calibration (e.g.  $X$  or  $Y$ ) was important – for gate durations  $t_X = n\tau_L$  ( $t_X = (n + 1/2)\tau_L$ ),  $n \in \mathbb{N}$ , we found that this pulse sequence behaved as expected when using  $Y$  ( $X$ ) rotations. Recall that for our commensurate implementation,  $Y$  gates have a duration  $\tau_L/2$  longer than  $X$  gates. This results in, for  $t_X = n\tau_L$  ( $t_X = (n + 1/2)\tau_L$ ), alternating  $Y$  ( $X$ ) pulse trains with identical waveforms for all gates (in contrast, the equivalent same-sign pulse trains correspond to the waveform for each subsequent gate being flipped). We hypothesize that, due to sequential pulses implementing rotations in opposite directions having the same waveform, long-time transients were suppressed rather than amplified in this calibration by the choice of  $X$  vs  $Y$  rotations.

3. **Precise amplitude calibration.** We used a pulse train looping over the set  $\{X_{\pi/2}, Y_{\pi/2}, X_{-\pi/2}, Y_{-\pi/2}\}$  measuring only trains with a multiple of 3 pulses (e.g.  $n_{\text{tot}} = 3n$ ,  $n \in \mathbb{N}$ ). This sequence implements a pseudo-identity gate (only an identity with perfect control) that is sensitive to the pulse amplitude. We also note that this sequence was sensitive to the pulse detuning. However, the pulse detuning was calibrated immediately preceding and no effective change was seen by changing this calibration to the more usual  $X_{\pi}^n$  train. This specific pulse sequence was chosen in order to treat  $X$  and  $Y$  pulses equally and mitigate any skewing of the optimal amplitude from e.g. unwanted amplification of transients from a homogeneous pulse train.

For circular gates, three additional calibrations were performed to determine 1) the relative phase offset, 2) the relative pulse delay, and 3) the precise relative amplitude between the charge and flux drives. The exact procedure is outlined below.

1. **Rough  $\pi$ -pulse amplitude calibration for charge and flux.** We applied a sequence  $X_{\pi} + X_{\pi}$  while sweeping the pulse amplitude and fit the resulting population of  $|1\rangle$  to a cosine function. The optimal  $\pi$ -pulse amplitude was then calculated as half the amplitude for the max population.
2. **Relative phase offset calibration.** We applied simultaneous charge and flux drives of equal strength (with relative amplitude set by the previous measurement) and measured Rabi oscillations while sweeping the relative phase. The offset phase was determined by fitting the data to Eq. (B6).
3. **Relative pulse delay calibration.** We applied an alternating  $X_{\pi}$  pulse train of nominally simultaneous charge and flux gates while sweeping the relative drive delay and the total number of pulses (constraining it to be odd) and setting  $\Delta\varphi = 0$ . The resulting interference pattern yielded maximal

population of  $|1\rangle$  when the pulse trains for charge and flux arrived at the qubit simultaneously.

4. **Pulse detuning calibration (coarse).** The optimal pulse detuning parameter for circular gates was found with the same routine as for linear gates, with the relative phase set to  $\Delta\varphi = \pi/2$  and enforcing  $\delta = \delta_{\text{charge}} = \delta_{\text{flux}}$ .
5. **Relative amplitude calibration.** We applied a nominally counter-rotating Rabi drive ( $\Delta\varphi = -\pi/2$ ) with a plateau equal to 3 times the pulse width as a function of the flux pulse amplitude (while keeping the charge amplitude fixed), resulting in minimal excited state occupation when the Rabi strengths of charge and flux were balanced.
6. **Pulse detuning calibration (fine).** As described in step 4.
7. **Precise amplitude calibration.** As described in the linear gate calibration, step 3.

## Appendix E: Gaussian Fitting of Calibration Scans: Gaussian Function as an Infinite Product

For multiple pulse parameters, optimal values were determined by fitting the product of pulse-train dataset line-cuts to a Gaussian function (in other words, multiplying the horizontal rows of a dataset which looks like Fig. 6(h), and fitting the resulting line). In this subsection, we justify this methodology and provide an infinite product expression of the Gaussian function  $e^{-x^2/2\sigma^2}$ .

For a pulse parameter  $x$ , we assume that at the optimal value  $x_{\text{opt}}$  applying a pseudo-identity gate comprised of a pulse train with  $n$  repetitions (e.g.  $(X_{\pi} + X_{-\pi})^n$ ) leaves the qubit in its initial state. However, a slightly offset value of  $x$  will lead to an over- or under-rotation of the qubit by an amount  $n\Delta\theta = nk(x - x_{\text{opt}})$  and a corresponding population of the excited state of  $p_{|0\rangle}^n = \frac{1}{2}(1 + \cos(n\Delta\theta))$ , where  $k$  is a constant of proportionality depending on the details of how the parameter  $x$  affects the qubit rotation. In our experiment,  $x$  corresponded to the pulse detuning or amplitude, but we note that this argument can be generalized to other parameters which effect the qubit rotation angle similarly.

In order to determine the optimal value  $x_{\text{opt}}$ , we took datasets measuring the excited state probability  $p_{|1\rangle}^n$  after pseudo-identity gates as a function of the number of repetitions  $n$  and the pulse parameter  $x$ . We then took the product for all different  $n$ , resulting in the signal  $s(x)$ ,

$$s(x) = \prod_{n=0}^N \frac{1}{2}(1 + \cos(n\Delta\theta)) \quad (\text{E1})$$

$$= \left( \prod_{n=0}^N \cos(n\Delta\theta) \right)^2. \quad (\text{E2})$$

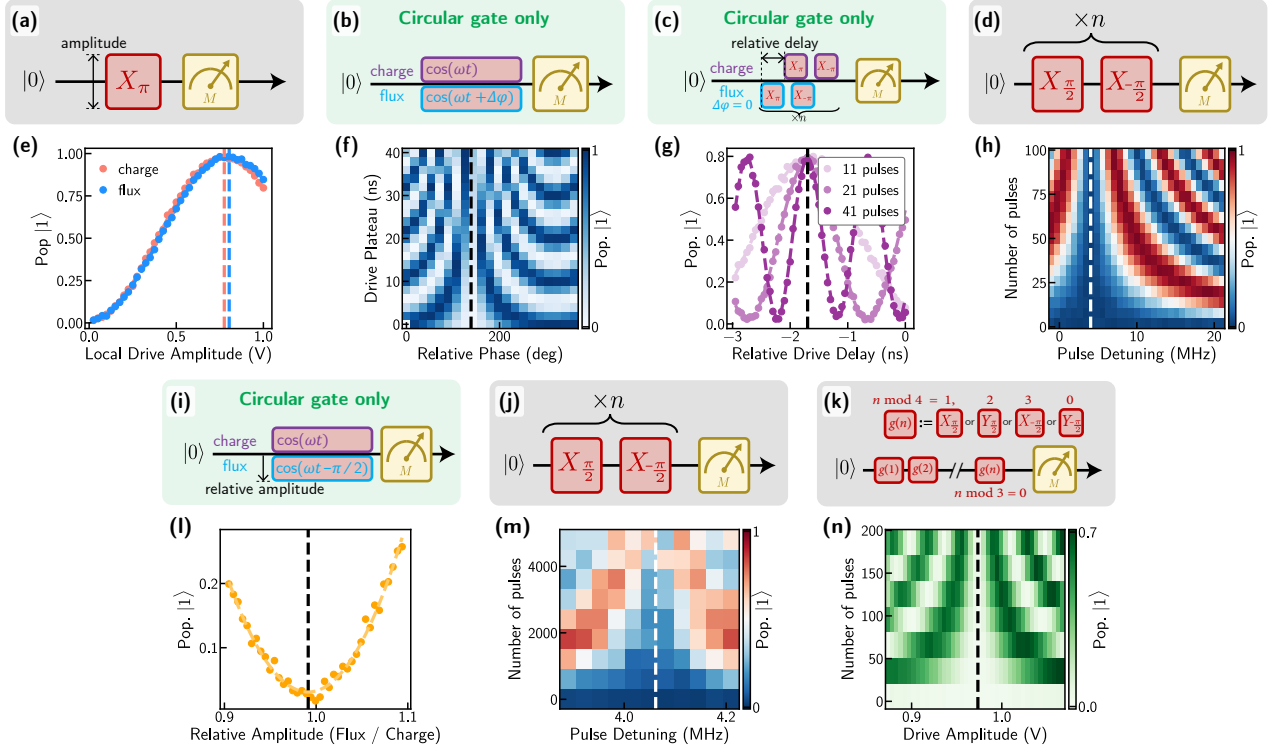


FIG. 6. **Measurement pulse sequences for single-qubit gate calibration.** (a-d),(i-k), (e-h),(l-n), respectively. (e) Rough pulse amplitude calibration. (f) Circular-only calibration for the relative phase between charge and flux drives. Marked in black is the counter-rotating relative phase. All circular gates were performed with the co-rotating phase ( $180^\circ$  offset from the counter-rotating phase). (g) Circular-only calibration for the relative delay between charge and flux pulses, to ensure pulses sent down both control lines arrived simultaneously at the qubit. (h) Rough pulse detuning calibration, primarily compensating for AC Stark shifts. (i) Circular-only fine calibration to balance the charge and flux drive strengths. (m) Fine pulse detuning calibration. (n) Fine pulse amplitude calibration.

In the limit as  $N \rightarrow \infty$ , one can show that such an infinite product converges exactly to a Gaussian when the cosine frequencies are weighted correctly,

$$\lim_{N \rightarrow \infty} \prod_{n=0}^N \cos\left(\frac{n}{N^{3/2}} \Delta\theta\right) = e^{-\Delta\theta^2/6}. \quad (\text{E3})$$

Even for small  $N$  (in our datasets,  $N \leq 5$ ), the above expression is easily fit to a Gaussian, giving an efficient and robust way to fit datasets such as Fig. 6(g,h,m,n).

## Appendix F: Gate Errors & Stability

### 1. Coherent and Incoherent Errors

To quantify the proportion of incoherent and coherent error in our gates, we performed purity randomized benchmarking (RB) [54, 55]. Our implementation of the pulse sequence included a recovery gate as in RB, followed by single-qubit state tomography. This enabled us to extract both the total and incoherent error per gate by

analyzing  $\langle \sigma_z \rangle$  and the purity  $P = \langle \sigma_x \rangle^2 + \langle \sigma_y \rangle^2 + \langle \sigma_z \rangle^2$  from the same dataset, respectively.

**RB analysis.** The total error per Clifford  $\epsilon$  was extracted by fitting the excited state population  $p_e$  by  $\langle p_e \rangle = A + Bu^m$  where  $\langle \cdot \rangle$  denotes the average over a collection of random sequences of  $m$  Cliffords,  $u = 1 - 2\epsilon$ , and  $A$  and  $B$  are constants determined by state preparation and measurement (SPAM) errors. The error per gate was then calculated by  $\epsilon_g = \epsilon/N$ , where  $N = 53/24 \approx 2.2083$  was the number of gates per Clifford given our native gateset  $\mathcal{G} = \{I, \pm X_{\pi/2}, \pm Y_{\pi/2}\}$ .

**Purity RB analysis.** The incoherent error per Clifford  $\epsilon_{\text{in}}$  was extracted by fitting the average state purity  $\langle P \rangle = A' + B'u'^m$ , where  $P = \langle \sigma_x \rangle^2 + \langle \sigma_y \rangle^2 + \langle \sigma_z \rangle^2$  is the state purity extracted by tomography after the  $m$ -Clifford RB sequence,  $u' = (1 - 2\epsilon_{\text{in}})^2$ , and similarly  $A'$  and  $B'$  are determined by SPAM errors. The incoherent error per gate was given by  $\epsilon_{g,\text{in}} = \epsilon_{\text{in}}/N$ .

We constructed an error budget for several commensurate charge and flux gates by measuring their total and incoherent errors as detailed above and quantifying the proportion of incoherent error from  $T_1$  and  $T_{2E}$  [Fig. 7]. Flux gates at times  $t_X \gtrsim 8$  ns were limited by incoher-

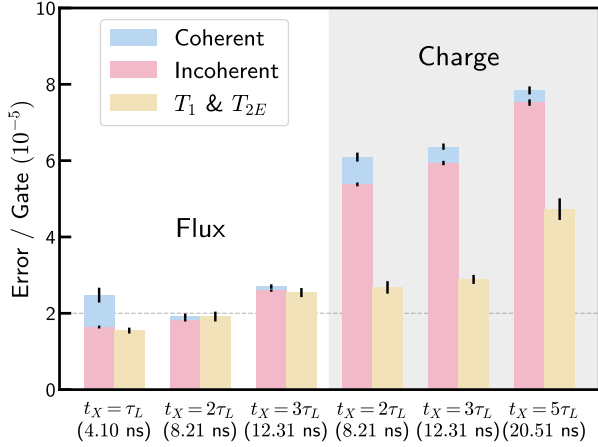


FIG. 7. **Error budget for commensurate charge and flux gates.** The total and incoherent error were measured through RB and purity RB, extracted from the same dataset for each gate as described in Appendix F 1. The estimated incoherent error from decoherence was also extracted from  $T_1$  and  $T_{2E}$  measurements taken immediately after each RB dataset. The coherent error budget item was determined by the difference between the total and incoherent errors. Black lines denote the uncertainty from parameter fits, with the error bar at the top of the coherent budget item corresponding to the total error uncertainty (extracted from the RB fit). Flux gates (white background) for times  $t_X \gtrsim 8$  ns were limited by qubit coherence, whereas charge gates (grey background) were largely limited by incoherent errors beyond undriven qubit decoherence.

ent errors, which could be attributed entirely (within uncertainty) to qubit decoherence. We note that for this dataset, the flux gate set with  $t_X = 2\tau_L$  represents our highest measured fidelity with a value of 99.99807(7)%. For our fastest flux gate ( $t_X = \tau_L \approx 4$  ns), coherent errors were found to play a more significant role, suggesting the breakdown of our calibration. Charge gates at all times were limited by incoherent errors, and the value could not be entirely accounted for by undriven qubit decoherence.

To probe the role of heating (from, e.g., power dissipated on the chip or in-line attenuators immediately before the device) on charge gate performance, we utilized a two-readout-pulse heralding scheme and swept the wait time between the readout pulses [Fig. 8]. At long wait times, we expect the relevant components to be in thermal equilibrium with the environment at the start of every qubit pulse sequence and provide no excess decoherence to the qubit. At short wait times, we expect the elements to heat during an experiment and provide a more severe source of qubit decoherence, which would contribute to incoherent error. The maximum wait time of 1600  $\mu$ s represents a duration of over 5x the longest pulse sequence used in the RB measurements. The  $t_X = 2\tau_L$  commensurate charge gate error displays an improvement until  $\approx 500$   $\mu$ s and then plateaus, with a maximum error reduction of  $\sim 20 - 30\%$ . The measured coherence times

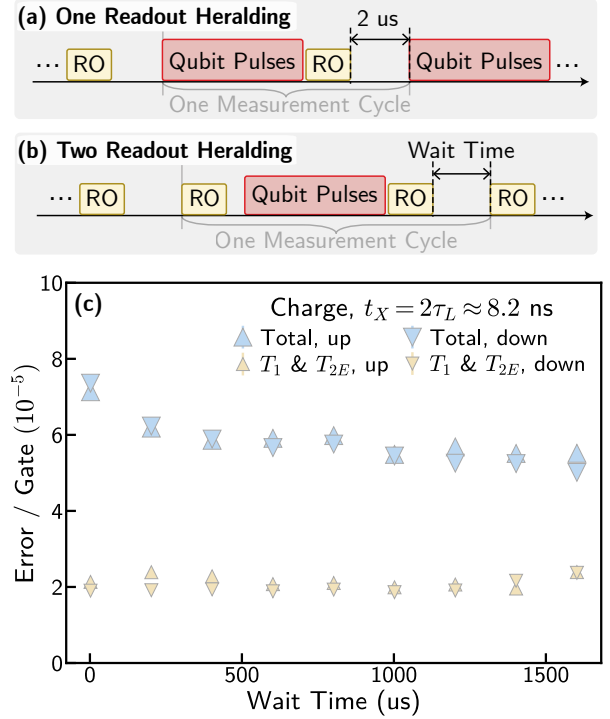


FIG. 8. **Charge gate heating characterization.** (a) One-readout-pulse heralding scheme, as used for all other data in this work. (b) Two-readout-pulse heralding scheme, as used for the experiment in this figure. The time between qubit pulses and the preceding readout pulse was kept 2  $\mu$ s. The time between readout pulses was swept in order to investigate the impact of heating on gate performance. (c) Total and  $T_1 + T_{2E}$  error for a commensurate charge gate with  $t_X = 2\tau_L \approx 8.2$  ns as a function of the wait time between readout pulses, using the pulse sequence of (b). The total error (blue) was measured through RB, and the  $T_1 + T_{2E}$  error (yellow) was extracted from  $T_1$  and  $T_{2E}$  measurements taken immediately after each RB dataset. Data is displayed from back-to-back sweeps of the wait time from 0 to 1600  $\mu$ s (upwards triangles) and then 1600  $\mu$ s to 0 (downwards triangles). The total error improved by 20 – 30% for wait times above 500  $\mu$ s, while the measured qubit coherence remained approximately constant.

remained approximately constant over the duration of the experiment, supporting our interpretation that the total error trend originated from mitigating system heating. At the longest wait time (least heating), we still find that our measured decoherence only accounts for at most  $\approx 45\%$  of the total error. We hypothesize that the remaining incoherent error for charge gates is due to leakage, enabled by the large charge matrix elements to higher levels (relative to that of the  $|0\rangle \leftrightarrow |1\rangle$  transition).

## 2. Stability

To investigate the stability of our system and gate parameters, we measured the total and incoherent error for

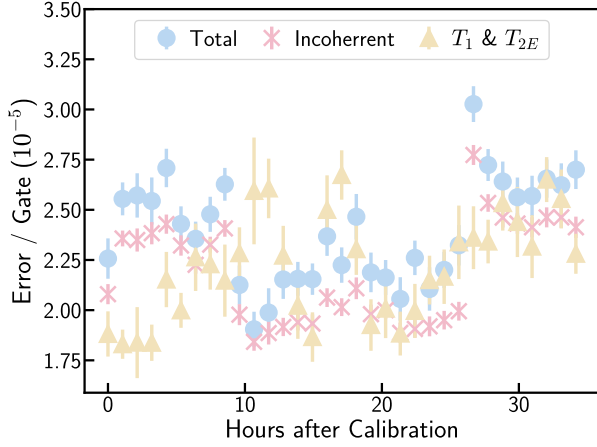


FIG. 9. **Stability for commensurate flux gates** ( $t_X = 2\tau_L \approx 8.2$  ns). The total and incoherent error per gate were measured through RB and purity RB, extracted from the same dataset as described in Appendix F 1. No significant drift or degradation of gate performance was observed.

a commensurate flux gate set with  $t_X = 2\tau_L \approx 8.2$  ns (with interleaved  $T_1$  and  $T_{2E}$  measurements) as a function of time after an initial calibration [Fig. 9]. Over a span of 34 hours after the initial calibration, the total error per gate fluctuated by less than  $1.13 \times 10^{-5}$ , and displayed no significant degradation.

### Appendix G: Comparison of Incommensurate Gates with Linear and Circular Drives

Here we present randomized benchmarking data comparing linear and circular driving schemes for incommensurate gates [Fig. 10]. To represent linear drives, we utilized the best linear driving scheme comprised of a purely flux drive. We present data for two separate gate durations,  $t_g = 1.2\tau_L \approx 4.9$  ns and  $t_g = 1.7\tau_L \approx 7.0$  ns. For  $t_g = 1.2\tau_L$ , we observe no benefit from circular driving over flux driving, suggesting the relevance of error channels beyond counter-rotating effects as  $t_g \rightarrow \tau_L$ , e.g., coherent leakage or the non-uniformity of AC Stark shifts. In contrast, for  $t_g = 1.7\tau_L$ , we observe that circular driving outperforms flux driving, signaling the benefit of circular driving for incommensurate single-qubit gates when counter-rotating errors dominate.

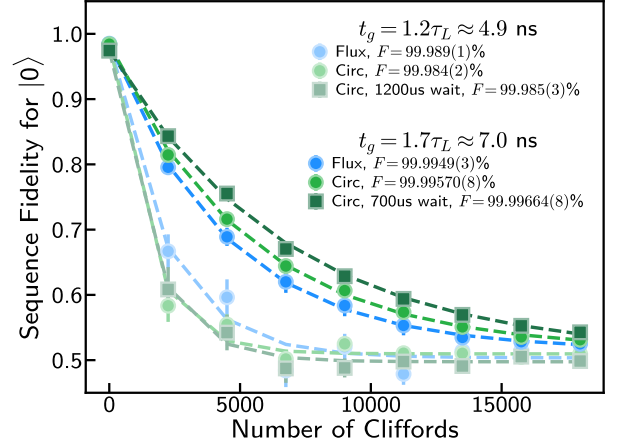


FIG. 10. **Comparison of incommensurate gates with linear and circular drives.** RB data for incommensurate gates utilizing a linearly polarized flux drive and a circularly polarized co-rotating drive is shown for two gate durations,  $t_g = 1.2\tau_L \approx 4.9$  ns and  $t_g = 1.7\tau_L \approx 7.0$  ns. We include data for circular drives with (square marker) and without (circular marker) additional wait times as defined in Fig. 8 in order to elucidate the efficacy of circular driving for suppressing counter-rotating errors while mitigating heating effects associated with the charge drive. For  $t_g = 1.2\tau_L$ , we observed no benefit from circular driving. For  $t_g = 1.7\tau_L$ , circularly polarized driving both with and without an additional wait time benefited gate performance relative to flux driving, which showed no benefit from an equivalent wait time.

- 
- [1] D. P. DiVincenzo, The Physical Implementation of Quantum Computation, *Fortschritte der Physik* **48**, 771 (2000).
- [2] Y. Nakamura, Y. A. Pashkin, and J. S. Tsai, Coherent control of macroscopic quantum states in a single-cooper-pair box, *Nature* **398**, 786 (1999).
- [3] J. Koch, T. M. Yu, J. Gambetta, A. A. Houck, D. I. Schuster, J. Majer, A. Blais, M. H. Devoret, S. M. Girvin, and R. J. Schoelkopf, Charge-insensitive qubit design derived from the cooper pair box, *Phys. Rev. A* **76**, 042319 (2007).
- [4] R. Barends, J. Kelly, A. Megrant, A. Veitia, D. Sank, E. Jeffrey, T. C. White, J. Mutus, A. G. Fowler, B. Campbell, *et al.*, Superconducting quantum circuits at the surface code threshold for fault tolerance, *Nature* **508**, 500 (2014).
- [5] F. Arute, K. Arya, R. Babbush, D. Bacon, J. C. Bardin, R. Barends, R. Biswas, S. Boixo, F. G. Brandao, D. A. Buell, *et al.*, Quantum supremacy using a programmable superconducting processor, *Nature* **574**, 505 (2019).
- [6] R. Acharya, I. Aleiner, R. Allen, T. I. Andersen, M. Ansmann, F. Arute, K. Arya, A. Asfaw, J. Atalaya, R. Babbush, *et al.*, Suppressing quantum errors by scaling a surface code logical qubit, *Nature* **614**, 676 (2023).
- [7] A. G. Fowler, M. Mariantoni, J. M. Martinis, and A. N. Cleland, Surface codes: Towards practical large-scale quantum computation, *Phys. Rev. A* **86**, 032324 (2012), publisher: American Physical Society.
- [8] D. Bluvstein, S. J. Evered, A. A. Geim, S. H. Li, H. Zhou, T. Manovitz, S. Ebadi, M. Cain, M. Kalinowski, D. Hangleiter, J. P. B. Atalides, N. Maskara, I. Cong, X. Gao, P. S. Rodriguez, *et al.*, Logical quantum processor based on reconfigurable atom arrays, *Nature* **626**, 58 (2023).
- [9] M. P. da Silva, C. Ryan-Anderson, J. M. Bello-Rivas, A. Chernoguzov, J. M. Dreiling, C. Foltz, F. Frachon, J. P. Gaebler, T. M. Gatterman, L. Grans-Samuelsson, D. Hayes, N. Hewitt, J. Johansen, D. Lucchetti, M. Mills, *et al.*, Demonstration of logical qubits and repeated error correction with better-than-physical error rates, [arXiv:2404.02280 \[quant-ph\]](https://arxiv.org/abs/2404.02280) (2024).
- [10] F. Motzoi, J. M. Gambetta, P. Rebentrost, and F. K. Wilhelm, Simple pulses for elimination of leakage in weakly nonlinear qubits, *Phys. Rev. Lett.* **103**, 110501 (2009).
- [11] D. Zhu, T. Jaako, Q. He, and P. Rabl, Quantum computing with superconducting circuits in the picosecond regime, *Phys. Rev. Appl.* **16**, 014024 (2021).
- [12] J. A. Schreier, A. A. Houck, J. Koch, D. I. Schuster, B. R. Johnson, J. M. Chow, J. M. Gambetta, J. Majer, L. Frunzio, M. H. Devoret, S. M. Girvin, and R. J. Schoelkopf, Suppressing charge noise decoherence in superconducting charge qubits, *Phys. Rev. B* **77**, 180502 (2008).
- [13] Z. Chen, J. Kelly, C. Quintana, R. Barends, B. Campbell, Y. Chen, B. Chiaro, A. Dunsworth, A. G. Fowler, E. Lucero, E. Jeffrey, A. Megrant, J. Mutus, M. Neeley, C. Neill, *et al.*, Measuring and Suppressing Quantum State Leakage in a Superconducting Qubit, *Phys. Rev. Lett.* **116**, 020501 (2016).
- [14] E. Hyyppä, A. Vepsäläinen, M. Papič, C. F. Chan, S. Inel, A. Landra, W. Liu, J. Luus, F. Marxer, C. Ockeloen-Korppi, S. Orbell, B. Tarasinski, and J. Heinsoo, Reducing leakage of single-qubit gates for superconducting quantum processors using analytical control pulse envelopes, [arXiv:2402.17757 \[quant-ph\]](https://arxiv.org/abs/2402.17757) (2024).
- [15] F. Bloch and A. Siegert, Magnetic Resonance for Nonrotating Fields, *Phys. Rev.* **57**, 522 (1940).
- [16] G. D. Fuchs, V. V. Dobrovitski, D. M. Toyli, F. J. Heremans, and D. D. Awschalom, Gigahertz dynamics of a strongly driven single quantum spin, *Science* **326**, 1520 (2009).
- [17] C. Avinadav, R. Fischer, P. London, and D. Gershoni, Time-optimal universal control of two-level systems under strong driving, *Phys. Rev. B* **89**, 245311 (2014).
- [18] C. Deng, J.-L. Orgiazzi, F. Shen, S. Ashhab, and A. Lupascu, Observation of floquet states in a strongly driven artificial atom, *Phys. Rev. Lett.* **115**, 133601 (2015).
- [19] D. Burgarth, P. Facchi, G. Gramegna, and K. Yuasa, One bound to rule them all: From Adiabatic to Zeno, *Quantum* **6**, 737 (2022).
- [20] D. Vion, A. Aassime, A. Cottet, P. Joyez, H. Pothier, C. Urbina, D. Esteve, and M. H. Devoret, Manipulating the quantum state of an electrical circuit, *Science* **296**, 886 (2002).
- [21] J. Mooij, T. Orlando, L. Levitov, L. Tian, C. H. Van der Wal, and S. Lloyd, Josephson persistent-current qubit, *Science* **285**, 1036 (1999).
- [22] T. P. Orlando, J. E. Mooij, L. Tian, C. H. van der Wal, L. S. Levitov, S. Lloyd, and J. J. Mazo, Superconducting persistent-current qubit, *Phys. Rev. B* **60**, 15398 (1999).
- [23] J. R. Friedman, V. Patel, W. Chen, S. K. Tolpygo, and J. E. Lukens, Quantum superposition of distinct macroscopic states, *Nature* **406**, 43 (2000).
- [24] C. H. van der Wal, A. C. J. ter Haar, F. K. Wilhelm, R. N. Schouten, C. J. P. M. Harmans, T. P. Orlando, S. Lloyd, and J. E. Mooij, Quantum superposition of macroscopic persistent-current states, *Science* **290**, 773 (2000).
- [25] V. E. Manucharyan, J. Koch, L. I. Glazman, and M. H. Devoret, Fluxonium: Single cooper-pair circuit free of charge offsets, *Science* **326**, 113 (2009).
- [26] F. Yan, S. Gustavsson, A. Kamal, J. Birenbaum, A. P. Sears, D. Hover, T. J. Gudmundsen, D. Rosenberg, G. Samach, S. Weber, *et al.*, The flux qubit revisited to enhance coherence and reproducibility, *Nat. Commun.* **7**, 1 (2016).
- [27] M. Yurtalan, J. Shi, G. Flatt, and A. Lupascu, Characterization of multilevel dynamics and decoherence in a high-anharmonicity capacitively shunted flux circuit, *Phys. Rev. Appl.* **16**, 054051 (2021).
- [28] A. Gyenis, A. Di Paolo, J. Koch, A. Blais, A. A. Houck, and D. I. Schuster, Moving beyond the Transmon: Noise-Protected Superconducting Quantum Circuits, *PRX Quantum* **2**, 030101 (2021).
- [29] I. M. Pop, K. Geerlings, G. Catelani, R. J. Schoelkopf, L. I. Glazman, and M. H. Devoret, Coherent suppression of electromagnetic dissipation due to superconducting quasiparticles., *Nature* **508**, 369 (2014).
- [30] L. B. Nguyen, Y.-H. Lin, A. Somoroff, R. Mencia, N. Grabon, and V. E. Manucharyan, High-coherence fluxonium qubit, *Phys. Rev. X* **9**, 041041 (2019).

- [31] A. Somoroff, Q. Ficheux, R. A. Mencia, H. Xiong, R. Kuzmin, and V. E. Manucharyan, Millisecond coherence in a superconducting qubit, *Phys. Rev. Lett.* **130**, 267001 (2023).
- [32] L. Ding, M. Hays, Y. Sung, B. Kannan, J. An, A. Di Paolo, A. H. Karamlou, T. M. Hazard, K. Azar, D. K. Kim, B. M. Niedzielski, A. Melville, M. E. Schwartz, J. L. Yoder, T. P. Orlando, S. Gustavsson, J. A. Grover, K. Serniak, and W. D. Oliver, High-fidelity, frequency-flexible two-qubit fluxonium gates with a transmon coupler, *Phys. Rev. X* **13**, 031035 (2023).
- [33] H. Zhang, C. Ding, D. Weiss, Z. Huang, Y. Ma, C. Guinn, S. Sussman, S. P. Chitta, D. Chen, A. A. Houck, J. Koch, and D. I. Schuster, Tunable inductive coupler for high-fidelity gates between fluxonium qubits, *PRX Quantum* **5**, 020326 (2024).
- [34] P. London, P. Balasubramanian, B. Naydenov, L. P. McGuinness, and F. Jelezko, Strong driving of a single spin using arbitrarily polarized fields, *Phys. Rev. A* **90**, 012302 (2014).
- [35] A. Laucht, S. Simmons, R. Kalra, G. Tosi, J. P. Dehollain, J. T. Muhonen, S. Freer, F. E. Hudson, K. M. Itoh, D. N. Jamieson, J. C. McCallum, A. S. Dzurak, and A. Morello, Breaking the rotating wave approximation for a strongly driven dressed single-electron spin, *Phys. Rev. B* **94**, 161302 (2016).
- [36] X. You, J. A. Sauls, and J. Koch, Circuit quantization in the presence of time-dependent external flux, *Phys. Rev. B* **99**, 174512 (2019).
- [37] J. Bryon, D. Weiss, X. You, S. Sussman, X. Croot, Z. Huang, J. Koch, and A. A. Houck, Time-dependent magnetic flux in devices for circuit quantum electrodynamics, *Phys. Rev. Appl.* **19**, 034031 (2023).
- [38] P. Krantz, M. Kjaergaard, F. Yan, T. P. Orlando, S. Gustavsson, and W. D. Oliver, A quantum engineer's guide to superconducting qubits, *Applied Physics Reviews* **6**, 021318 (2019).
- [39] I. I. Rabi, N. F. Ramsey, and J. Schwinger, Use of Rotating Coordinates in Magnetic Resonance Problems, *Rev. Mod. Phys.* **26**, 167 (1954).
- [40] An analogous example of physics that depends on the stability of the relative phase between the carrier and envelope of few-cycle pulses can be found in ultrafast optics [56, 57].
- [41] D. L. Campbell, Y.-P. Shim, B. Kannan, R. Winik, D. K. Kim, A. Melville, B. M. Niedzielski, J. L. Yoder, C. Tahan, S. Gustavsson, and W. D. Oliver, Universal nonadiabatic control of small-gap superconducting qubits, *Phys. Rev. X* **10**, 041051 (2020).
- [42] I. N. Moskalenko, I. A. Simakov, N. N. Abramov, D. O. Moskalev, A. A. Pishchimova, N. S. Smirnov, E. V. Zikiy, I. A. Rodionov, and I. S. Besedin, High fidelity two-qubit gates on fluxoniums using a tunable coupler, *npj Quantum Information* **8** (2022).
- [43] D. C. McKay, C. J. Wood, S. Sheldon, J. M. Chow, and J. M. Gambetta, Efficient z gates for quantum computing, *Phys. Rev. A* **96**, 022330 (2017).
- [44] E. Magesan, J. M. Gambetta, and J. Emerson, Scalable and robust randomized benchmarking of quantum processes, *Phys. Rev. Lett.* **106**, 180504 (2011).
- [45] E. Magesan, J. M. Gambetta, B. R. Johnson, C. A. Ryan, J. M. Chow, S. T. Merkel, M. P. da Silva, G. A. Keefe, M. B. Rothwell, T. A. Ohki, M. B. Ketchen, and M. Steffen, Efficient measurement of quantum gate error by interleaved randomized benchmarking, *Phys. Rev. Lett.* **109**, 080505 (2012).
- [46] Z. Li, P. Liu, P. Zhao, Z. Mi, H. Xu, X. Liang, T. Su, W. Sun, G. Xue, J.-N. Zhang, W. Liu, Y. Jin, and H. Yu, Error per single-qubit gate below  $10^{-4}$  in a superconducting qubit, *npj Quantum Information* **9**, 1 (2023).
- [47] H. Zhang, S. Chakram, T. Roy, N. Earnest, Y. Lu, Z. Huang, D. K. Weiss, J. Koch, and D. I. Schuster, Universal fast-flux control of a coherent, low-frequency qubit, *Phys. Rev. X* **11**, 011010 (2021).
- [48] D. Weiss, H. Zhang, C. Ding, Y. Ma, D. I. Schuster, and J. Koch, Fast high-fidelity gates for galvanically-coupled fluxonium qubits using strong flux modulation, *PRX Quantum* **3**, 040336 (2022).
- [49] N. Earnest, S. Chakram, Y. Lu, N. Irons, R. K. Naik, N. Leung, L. Ocola, D. A. Czaplewski, B. Baker, J. Lawrence, J. Koch, and D. I. Schuster, Realization of a  $\Lambda$  system with metastable states of a capacitively shunted fluxonium, *Phys. Rev. Lett.* **120**, 150504 (2018).
- [50] Q. Ficheux, L. B. Nguyen, A. Somoroff, H. Xiong, K. N. Nesterov, M. G. Vavilov, and V. E. Manucharyan, Fast logic with slow qubits: microwave-activated controlled-z gate on low-frequency fluxoniums, *Phys. Rev. X* **11**, 021026 (2021).
- [51] E. Dogan, D. Rosenstock, L. Le Guevel, H. Xiong, R. A. Mencia, A. Somoroff, K. N. Nesterov, M. G. Vavilov, V. E. Manucharyan, and C. Wang, Two-fluxonium cross-resonance gate, *Phys. Rev. Appl.* **20**, 024011 (2023).
- [52] K. N. Nesterov, Q. Ficheux, V. E. Manucharyan, and M. G. Vavilov, Proposal for entangling gates on fluxonium qubits via a two-photon transition, *PRX Quantum* **2**, 020345 (2021).
- [53] D. Sank, M. Khezri, S. Isakov, and J. Atalaya, Balanced coupling in electromagnetic circuits, Private Communication (2024).
- [54] J. Wallman, C. Granade, R. Harper, and S. T. Flammia, Estimating the coherence of noise, *New Journal of Physics* **17**, 113020.
- [55] G. Feng, J. J. Wallman, B. Buonacorsi, F. H. Cho, D. K. Park, T. Xin, D. Lu, J. Baugh, and R. Laflamme, Estimating the Coherence of Noise in Quantum Control of a Solid-State Qubit, *Phys. Rev. Lett.* **117**, 260501.
- [56] T. Brabec and F. Krausz, Intense few-cycle laser fields: Frontiers of nonlinear optics, *Rev. Mod. Phys.* **72**, 545 (2000).
- [57] A. Baltuška, T. Udem, M. Uiberacker, M. Hentschel, E. Goulielmakis, C. Gohle, R. Holzwarth, V. S. Yakovlev, A. Scrinzi, T. W. Hänsch, and F. Krausz, Attosecond control of electronic processes by intense light fields, *Nature* **421**, 611 (2003).